A High-Efficiency Solar Array Simulator Implemented by an *LLC* Resonant DC–DC Converter

Chien-Hsuan Chang, *Member, IEEE*, En-Chih Chang, and Hung-Liang Cheng, *Member, IEEE*

***Abstract*—In this paper, a high-efficiency solar array simulator (SAS) implemented by an *LLC* resonant dc–dc converter is proposed to save the cost and energy of photovoltaic (PV) system testing. The proposed converter has zero-voltage switching (ZVS) operation of the primary switches and zero-current switching (ZCS) operation of the rectifier diodes. By frequency modulation control, the output impedance of an *LLC* resonant converter can be regulated from zero to infinite without shunt or serial resistors. Therefore, the efficiency of the proposed SAS can be significantly increased. The circuit operations are analyzed in detail to derive the theoretical equations. Circuit parameters are designed based on the practical considerations. Finally, an illustrative example is implemented to demonstrate the feasibility of the proposed SAS.**

***Index Terms*—*LLC* resonant dc–dc converter, photovoltaic (PV) system, solar array simulator (SAS).**

I. Introduction

RECENTLY, residue of traditional energy resources (i.e., fossil energy) is highly limited and would be exhausted in the near future. Besides, combustion of fossil fuels results in a serious threat of global warming. Hence, developing renewable energy resources to replace traditional ones has been a research of great urgency. Among all renewable energy resources, photovoltaic (PV) energy becomes most attractive recently, because it is noiseless, pollution-free, nonradioactive, and inexhaustible. Since the output PV characteristics are influenced by illumination and temperature, the maximum power point tracking (MPPT) [1], [2] is a necessary technology in PV applications.

Atmospheric conditions are uncontrollable so that PV system engineers cannot obtain the corresponding PV characteristics to qualify the feasibility and dynamic response of their MPPT approaches immediately. In order to relieve this difficulty, metal-halide lamps and temperature controlling devices are used to control the illumination and temperature of PV arrays [3], [4]. But the temperature controlling devices are very expensive, and the power consumption of driving metal-halide lamps results in additional energy waste. Therefore, the literatures [5]–[11] propose several solar array simulators (SASs) which can provide PV characteristics directly. Among them, the most applicable approach in high-power systems is using pulse width modulation (PWM) dc–dc converters to generate PV characteristics [8]–[11]. However, shunt resistors are required to limit output voltage at extremely high duty-ratio, and serial resistors are used to inhibit spike current at extremely low duty-ratio operation. These resistors cause additional power dissipations and lower conversion efficiency. Furthermore, the power switches of PWM converters operate in hard switching, which will result in high switching losses and electromagnetic interference (EMI) issues.

Theoretically, the output impedance of resonant converters can be regulated from zero to infinite by applying frequency modulation control [12]. Because it can match that of PV output characteristics without shunt or serial resistors, resonant converters are more applicable than the traditional PWM dc–dc converters for the SAS applications.

Among numerous resonant converters, the series resonant converter (SRC) provides satisfied efficiency, but it has the problem of output voltage regulation at light load condition [13], [14]. Although the parallel resonant converter (PRC) has no light load regulation issue, its circulating energy is much higher than SRC and impacts efficiency significantly [14], [15]. The series-parallel resonant converter (SPRC) remains the advantages of SRC and PRC, which are smaller circulating energy and not so sensitive to load change [16], [17]. However, the same as SRC and PRC, SPRC requires operating at very high switching frequency to obtain extremely low output-voltage. Therefore, with low output-voltage operation, all of SRC, PRC, and SPRC possess high circulating energy to lower their efficiencies.

This paper proposes to implement a high-efficiency SAS by an *LLC* resonant dc–dc converter. At high input-voltage or low output-voltage operation, the *LLC* resonant converter has smaller circulating energy than SRC, PRC, and SPRC [18], [19]. Both the active switches of this converter can turn ON with zero-voltage switching (ZVS), and both the output rectifier diodes can turn OFF with zero-current switching (ZCS), which results in higher conversion efficiency. By applying frequency modulation control, the output impedance of an *LLC* converter can be regulated from zero to infinite without shunt or serial resistors [12], [18]; hence, the efficiency of the proposed SAS can be significantly increased. By the way, this converter has a transformer to provide electrical isolation for safety requirements.

In this paper, the theoretical equations and operation principles of the *LLC* resonant converter will be introduced. Circuit parameters are designed based on the practical considerations. Finally, an illustrative example is implemented to demonstrate the feasibility of the proposed high-efficiency SAS.

Manuscript received May 15, 2012; revised June 13, 2012; accepted June 13, 2012. Date of current version December 7, 2012. This work was supported by the National Science Council (NSC) of Taiwan, Taiwan, under Grant NSC-98-2221-E-214-068. Recommended for publication by Associate Editor T. Suntio.

The authors are with the Department of Electrical Engineering, I-Shou University, Kaohsiung 84001, Taiwan (e-mail: chchang@isu.edu.tw; enchihchang@isu.edu.tw; hlcheng@isu.edu.tw).

Color versions of one or more of the figures in this paper are available online at http://ieeexplore.ieee.org.

Digital Object Identifier 10.1109/TPEL.2012.2205273

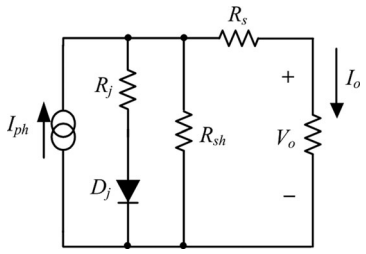

Fig. 1. Equivalent circuit of a solar cell.

II. Characteristics of Solar Cells

Solar cells are basically p–n junction semiconductors which transform solar energy into electricity directly. Fig. 1 shows an equivalent circuit of a solar cell [2], in which $R_{\rm sh}$ and R_s are the intrinsic shunt and serial resistors of the cell, respectively. A current source $I_{\rm ph}$ represents the cell photocurrent, which is a function of illumination S_i and solar array temperature T, and can be expressed as follows:

$$I_{\rm ph} = \frac{[I_{\rm SSO} + K_i(T - T_r)]S_i}{100} \tag{1}$$

where $I_{\rm sso}$ is the short-circuit current at reference temperature T_r and reference illumination (100 mW/cm^2), and K_i is temperature coefficient of the short-circuit current. Additionally, D_j expresses the p–n junction of a solar cell, and R_j is its nonlinear resistance. $I_{\rm sat}$ represents the reversed saturation current of D_j and can be expressed as follows:

$$I_{\rm sat} = I_{\rm rr}\left[\frac{T}{T_r}\right]^3 \exp\left[\frac{qE_G}{kA}\left(\frac{1}{T_r} - \frac{1}{T}\right)\right] \tag{2}$$

where $I_{\rm rr}$ is the corresponding reversed saturation current at T_r, $E_{\rm Gap}$ is the band-gap energy of the semiconductor used in the cell, q is charge of an electron (1.6×10^{-19} C), k is Boltzmann's constant (1.38×10^{-23} J/K), and A is the ideality factor of the p–n junction.

If there are n_s cells connected in series and n_p cells connected in parallel, the output characteristic of PV arrays can be represented by the following equations:

$$I_o = n_p I_{\rm ph} - n_p I_{\rm sat}\left[\exp\left(\frac{q}{kTA}\frac{V_o - I_o R_s}{n_s}\right) - 1\right] - \frac{V_o - I_o R_s}{R_{\rm sh}} \tag{3}$$

$$P_o = V_o I_o. \tag{4}$$

III. Analysis of the *LLC* Resonant DC–DC Converter

The circuit diagram of an *LLC* resonant dc–dc converter is shown in Fig. 2, which consists of an *LLC* resonant inverter, a current-driven transformer with a center-tapped rectifier. The topology of *LLC* converter is very similar to that of SRC. The main difference is that the magnetizing inductance L_m is only slightly higher than the resonant inductance L_r in the *LLC* converter. Therefore, at some load conditions, L_m may participate in the resonance with L_r and C_r and change the characteristics of resonant tank.

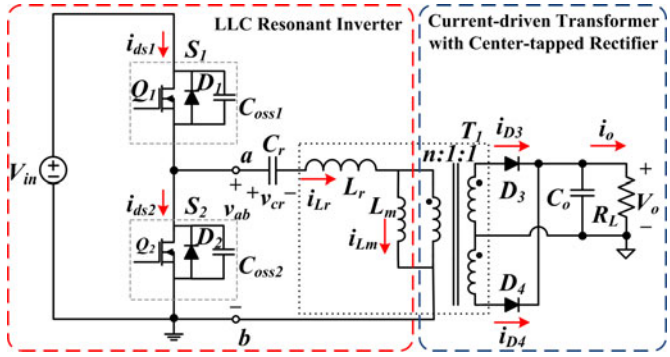

Fig. 2. Circuit diagram of *LLC* resonant dc/dc converter.

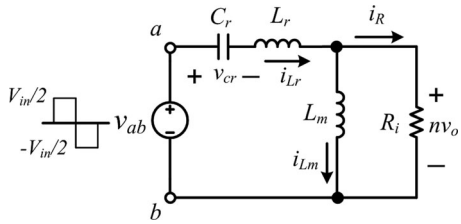

Fig. 3. Equivalent circuit of the *LLC* resonant converter.

The equivalent circuit of the *LLC* resonant inverter can be depicted as shown in Fig. 3, in which R_i is equivalent load resistance seen in primary side, and can be expressed as $R_i = 8n^2 R_L/\pi^2$. The input symmetrical square waveform $v_{\rm ab}$ with the magnitude of $V_{\rm in}/2$ can be obtained by alternate conducting of power switches S_1 and S_2. The transfer function of output voltage can be determined as (5) shown at the bottom of the next page, where the inductance ratio A, the second resonant frequency ω_L, and the load quality factor Q_L are defined as

$$A = \frac{L_r}{L_m} \tag{6}$$

$$\omega_L = 2\pi f_L = \frac{1}{\sqrt{(L_r + L_m)\cdot C_r}} \tag{7}$$

$$Q_L = R_i \times \sqrt{\frac{C_r}{L_r + L_m}} = R_i \cdot \omega_L \cdot C_r. \tag{8}$$

According to (5), the frequency response of output voltage gain of the *LLC* resonant converter can be illustrated in Fig. 4. It can be observed that there are two resonant frequencies. The second resonant frequency ω_L has been defined in (7), and the main resonant frequency ω_H can be determined as follows:

$$\omega_H = 2\pi f_H = \frac{1}{\sqrt{L_r \cdot C_r}}. \tag{9}$$

Fig. 4 can be divided into three operation regions according to the resonant frequencies of ω_H and ω_L. Because the impedance of resonant tank is capacitive in Region 3, the primary switches can operate under ZCS condition. But the current spike during turn-on transient will result in high-current

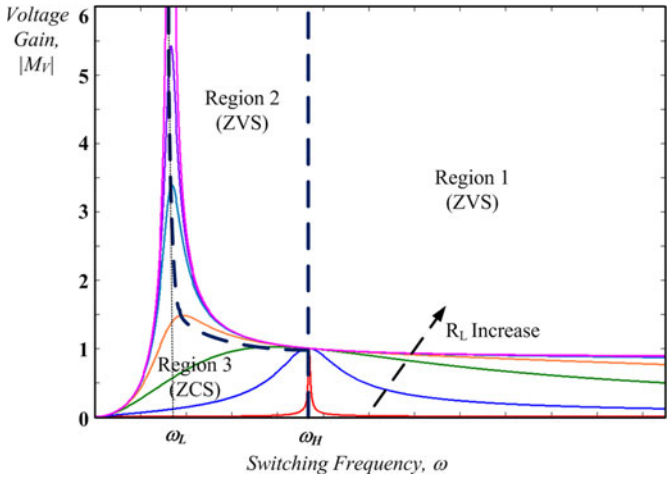

Fig. 4. Frequency response of output voltage gain of the *LLC* resonant converter.

stress and high-switching loss. Therefore, *LLC* resonant converters should be prevented from operating in this region [19], [20].

In region 1, the switching frequency is higher than the resonant frequency ω_H. The impedance of resonant tank is inductive so that the switches can operate under ZVS condition to reduce switching loss. Since voltage gain is always less than 1, the converter could be regarded as buck type. The operation principle in this region is very similar to SRC; hence, secondary rectifier diodes cannot operate under ZCS. Voltage spike will occur during turn-off transient and results in high switching loss.

According to Fig. 4, the switching frequency is lower than the main resonant frequency ω_H in region 2, in which the converter is regarded as boost type (voltage gain $\geqq 1$). During the main resonant period, because the voltage of L_m is clamped by output voltage, the inductor current i_{Lm} is linearly increasing. While i_{Lm} reaches the same level as the resonant current i_{Lr}, a second resonance with the frequency ω_L determined by C_r and ($L_r + L_m$) occurs. This resonance will continue until the primary switches switching again so that the converter can still operate under ZVS in region 2. Besides, during the second resonant period, the current of secondary rectifier diodes remains zero; hence, they can turn OFF naturally under ZCS condition [19], [20].

Theoretically, the optimal converter efficiency should be obtained in the point of switching frequency equal to the second resonant frequency ω_L. For practical considerations, in order to minimize power dissipation of SAS and prevent the operation point from entering region 3, the switching frequency of SAS operating in maximum output power should be designed as slightly higher than resonant frequency ω_L.

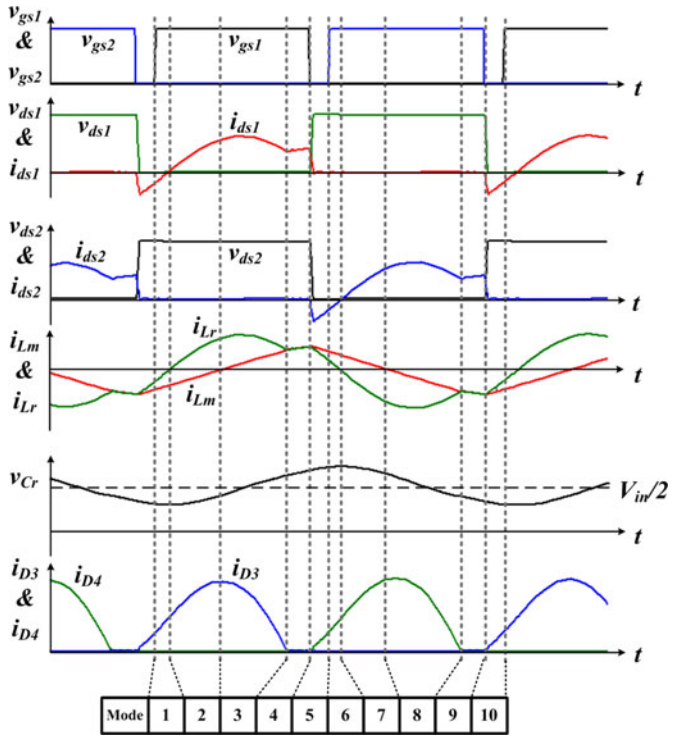

Fig. 5. Main waveforms of the *LLC* resonant converter operating in region 2.

IV. Operation Principles of the *LLC* Resonant DC–DC Converter

As shown in Fig. 2, the primary switches S_1 (S_2) are composed of an MOSFET Q_1 (Q_2), and its intrinsic antiparallel diode D_1 (D_2) and equivalent output capacitor C_{OSS1} (C_{OSS2}). The resonant tank is formed by the resonant capacitor C_r, and the leakage inductor L_r and magnetizing inductor L_m of the transformer T_1. By conducting the switches S_1 and S_2 alternately, a symmetrical square waveform with the magnitude of $V_{in}/2$ can be obtained in the input terminal of the resonant tank, where V_{in} is the input voltage. The center-tapped rectifier is constructed by connecting diodes D_3 and D_4 to the secondary windings of T_1.

Based on the analysis of earlier section, the main theoretical waveforms of the *LLC* resonant converter operating in region 2 are shown in Fig. 5. There are ten operation modes within one switching period. Because the waveforms are symmetrical, only the operation principles of the first five modes are introduced referring to the equivalent circuits shown in Fig. 6.

A. Mode 1

This mode starts when the switch S_1 is turned ON under ZVS. The equivalent circuit is shown in Fig. 6(a). The resonant current i_{Lr} is sine-wave and increases from negative to discharge C_r,

$$|M_V(\omega)| = \left|\frac{V_o}{V_{in}}\right| = \frac{1}{2n\left\{\sqrt{(1+A)^2\left[1-(\omega_L/\omega)^2\right]^2 + (1/Q_L)^2((\omega/\omega_L)(A/(1+A)) - (\omega_L/\omega))^2}\right\}} \quad (5)$$

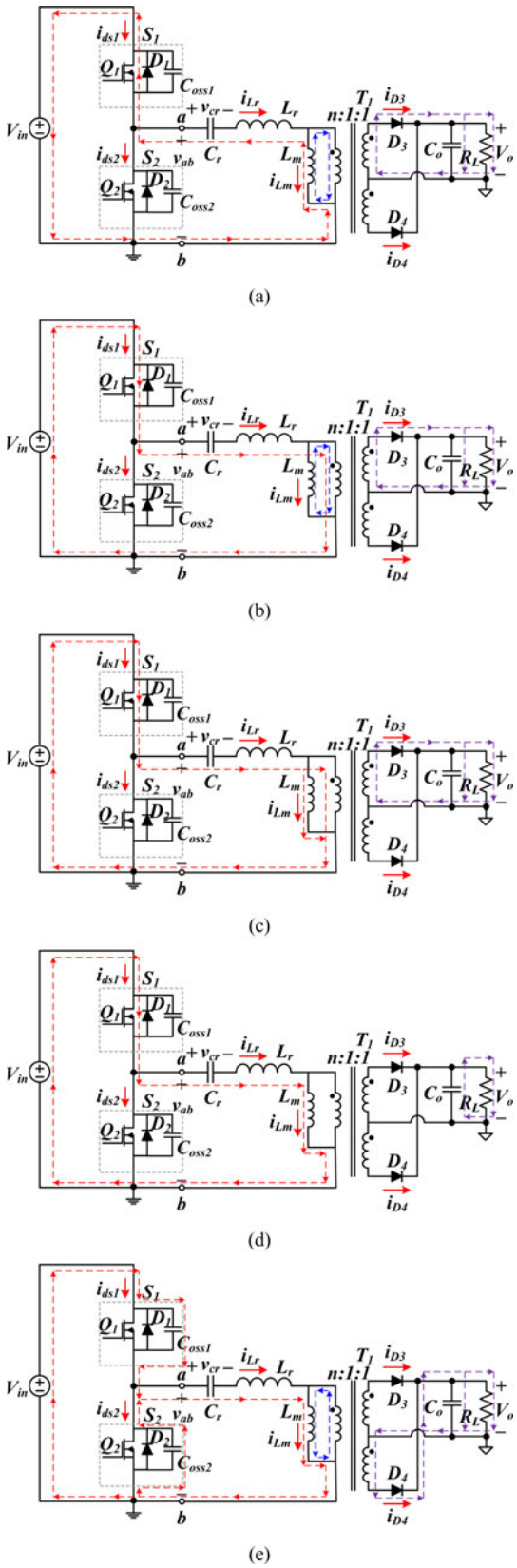

Fig. 6. Equivalent circuits of (a) Mode 1, (b) Mode 2, (c) Mode 3, (d) Mode 4, and (e) Mode 5 for the *LLC* converter operating in region 2.

and energy returns to the input voltage source. The voltage of L_m is clamped to nV_O so that the magnetizing current i_{Lm} increases linearly from negative. The energy stored in L_m will be released through D_3 to output load. When i_{Lr} reaches zero, this mode ends.

B. Mode 2

As shown in Fig. 6(b), since i_{Lr} increases from zero to positive, the input voltage source charges C_r and L_r, and supplies energy to output load simultaneously. The energy in L_m is released to output load continuously. When i_{Lm} reaches zero, this mode ends.

C. Mode 3

At this mode, because the voltage of L_m is still clamped to nV_O, i_{Lm} remains increasing linearly. The input voltage source charges L_m and supplies energy to output load. The equivalent circuit is shown in Fig. 6(c).

D. Mode 4

This mode starts when i_{Lr} and i_{Lm} equal each other. Current circulating through the secondary diode D_3 naturally decreases to zero so that this diode turns OFF under ZCS condition. The voltage spike caused by diode reverse recovery would not exist. The voltage of L_m is no longer clamped to nV_O, hence, L_m is in series with L_r and participates in the resonance with C_r. The equivalent circuit of this mode is shown in Fig. 6(d). Because the equivalent inductance of $(L_r + L_m)$ is higher than L_r, as shown in Fig. 5, i_{Lr} and i_{Lm} are almost constant in this short time interval.

E. Mode 5

As shown in Fig. 6(e), while S_1 is turning OFF, the resonant current i_{Lr} is charging C_{OSS1} and discharging C_{OSS2} simultaneously. At the moment of v_{ds2} decreasing to zero, the resonant current i_{Lr} flows through antiparalleled diode D_2 which provide ZVS operation for S_2 turn ON. At the same time, the secondary rectifier diode D_4 turns ON. The voltage of L_m is clamped to nV_O with reverse polarity so that the current i_{Lm} becomes decreasing linearly. The magnetizing inductor L_m is separated from the resonance with C_r. When S_2 turns ON under ZVS, this mode ends and enters the half cycle with symmetrical operation principles.

V. Design Specifications and Considerations

To verify the feasibility of the proposed SAS implemented by an *LLC* resonant converter, an illustrative example is built to provide the electrical characteristics of the PV module F-MSN-75W-R-02 (Motech Company, Ltd.). Considering the normal operation temperature of 25 °C and the maximum illumination of 80 mW/cm^2, the electrical characteristics of F-MSN-75W-R-02 can be determined from (1) to (4) and shown in Table I. Hence, the output specifications of the SAS are defined as 59 W, 0–21 V, and 0–4 A.

TABLE I
ELECTRICAL CHARACTERISTICS OF THE PV MODULE F-MSN-75W-R-02 AT 80 mW/cm^2 AND 25 °C

F-MSN-75W-R-02 at 80mW/cm^2 and 25°C	
Maximum Power, P_{max}	59 W
Voltage of Maximum Power Point, V_{mpp}	18 V
Current of Maximum Power Point, I_{mpp}	3.3 A
Voltage of Open Circuit Point, V_{OC}	21 V
Current of Short Circuit Point, I_{SC}	4 A

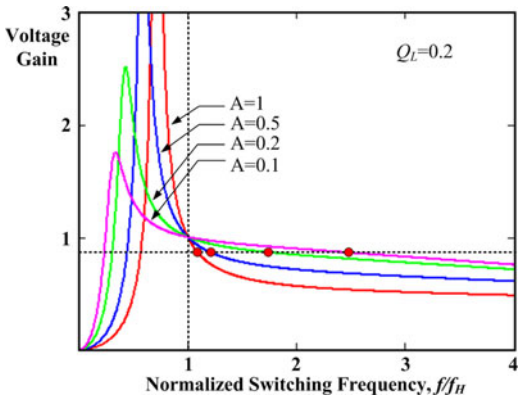

Fig. 7. Frequency response of output voltage gain with different inductor ratios.

Considering the problems of current harmonic distortions induced by rectifiers, the proposed SAS is designed to operate with an active power factor corrector in the front end. Therefore, its input voltage is set at 400 V_{dc}. The main resonant frequency f_H is determined at 100 kHz. The design considerations for component parameters are introduced as follows.

A. Inductor Ratio ($A = L_r / L_m$)

Since the output voltage of the SAS is from 0 to 21 V, the *LLC* resonant converter should operate in both regions 1 and 2. According to (5), Fig. 7 shows the frequency response of voltage gain related to different inductor ratio. In region 1, if the inductor ratio is higher, the lower voltage gain can be easily obtained by increasing frequency slightly. However, high-inductor ratio results in sharp slope of voltage gain in region 2, which might impact the stability of frequency modulation control. For tradeoff, the inductor ratio *A* is set at 0.5. Hence, the secondary resonant frequency f_L can be calculated from (7) and (9) to be 57.7 kHz.

B. Turn Ratio of Transformer

Based on the previous analysis, the optimal efficiency of an *LLC* resonant converter is located in region 2. To ensure that the converter operates in region 2 at maximum power condition, we set switching frequency equal to the main resonant frequency ($f = f_H$) when the output voltage $V_o = 14$ V. Considering duty ratio $D = 0.5$ and diode forward voltage $V_F = 0.7$ V, the minimum turn ratio can be determined from

$$n \geq \frac{V_{\text{in}} \cdot D}{(V_o + V_F)} \cong 13.6. \tag{10}$$

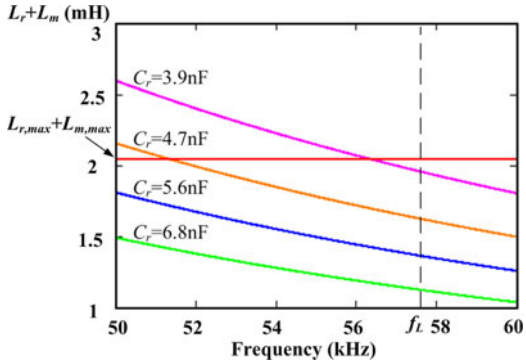

Fig. 8. Relation curves of C_r, $(L_r + L_m)$ and resonant frequency.

We select $n = 14$ in this design.

C. Components of Resonant Tank (L_m, L_r, and C_r)

The magnetizing inductor L_m should meet the condition expressed in (11) so that the primary switches can turn ON under ZVS [21], [22]

$$L_m \leq \frac{nV_oT_s \cdot t_{d,\min}}{8C_{\text{oss}}V_{\text{in}}}. \tag{11}$$

In the illustrative example, the equivalent output capacitance of power MOSFETs C_{oss} is 90 nF, and the minimum dead time $t_{d,\min}$ is 200 ns. Therefore, the maximum inductance of L_m can be expressed as follows:

$$L_{m,\max} = \frac{n \cdot V_o \cdot T_s \cdot t_{d,\min}}{8 \cdot V_{\text{in}} \cdot C_{\text{oss}}} = 1.36 \text{ mH}. \tag{12}$$

According to the definition of inductor ratio ($A = L_r/L_m$), the maximum inductance of L_r can also be determined as follows:

$$L_{r,\max} = A \cdot L_{m,\max} = 680.6\ \mu\text{H}. \tag{13}$$

According to (7), the relation curves of C_r, $(L_r + L_m)$ and the resonant frequency are illustrated in Fig. 8. From (12) and (13), the limit line of the maximum inductance of $(L_r + L_m)$ is also indicated in this figure. It can be observed that there are several standard capacitances to obtain the desired f_L with 57.7 kHz. C_r is chosen as 3.9 nF in this case. Hence, $L_r = 650\ \mu$H and $L_m = 1.3$ mH can be obtained from (7) and (9).

VI. EXPERIMENTAL RESULTS

Based on the previous design, the electrical specifications and component parameters of the *LLC* resonant converter are summarized in Table II. For convenience to explain the experimental results, the theoretical *V–I* curve of F-MSN-75W-R-02 at 80 mW/cm^2 and 25 °C is shown in Fig. 9(a), in which the dots, from "A" to "H," indicate operation points in this curve. By the way, all points are also depicted in the frequency response of output voltage, as shown in Fig. 9(b). It can be observed that points "D," "E," and "F" are located in region 2 to obtain high efficiency in high output-power operations.

Fig. 10 shows the voltage and current waveforms of the primary switches S_1 and S_2, when the SAS operates at the maximum power point (MPP) (point "E") and two extreme points

TABLE II
ELECTRICAL SPECIFICATIONS AND COMPONENT PARAMETERS OF THE ILLUSTRATIVE EXAMPLE

Electrical Specifications	
Input Voltage, V_{in}	400V
Output Voltage, V_O	0 – 21V
Output Current, I_O	0 – 4A
Maximum Power, P_O	60W
Main Resonant Frequency, f_H	100 kHz
Secondary Resonant Frequency, f_L	57.7 kHz
Switching Frequency	60 – 250 kHz
Component Parameters	
Resonant Inductor, L_r	650 μH
Magnetizing Inductor, L_m	1.3 mH
Resonant Capacitor, C_r	3.9 nF
Transformer Turn Ratio, n:1:1	14:1:1
Primary Switch, S_1 and S_2	STP10NK60Z
Rectifier Diode, D_3 and D_4	STPS3045CW

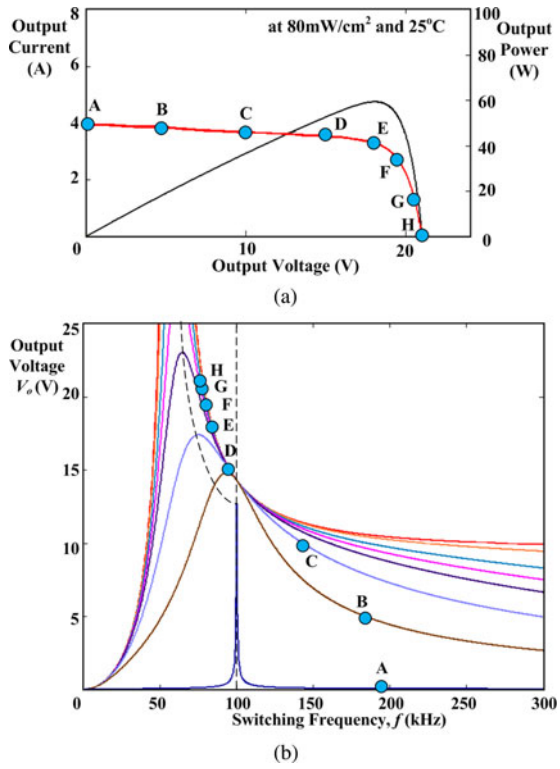

Fig. 9. Related operation points indicated in (a) the *V–I* curve and (b) the frequency response of output voltage.

(points "A" and "H"), respectively. They could be observed that S_1 and S_2 can turn ON under ZVS condition at all operation conditions. Besides, when the SAS operates at point "E" with high-output power, the turn-off current can be reduced by the second resonance, as shown in Fig. 10(a). Therefore, the circulating energy and turn-off loss can be significantly minimized to improve system efficiency.

Fig. 11 shows the measured efficiencies according to the operation points (from "A" to "H") marked at the theoretical *V–I* curve. The maximum system efficiency is up to around 92.5% and occurs at the MPP "E," resulting in energy saving significantly.

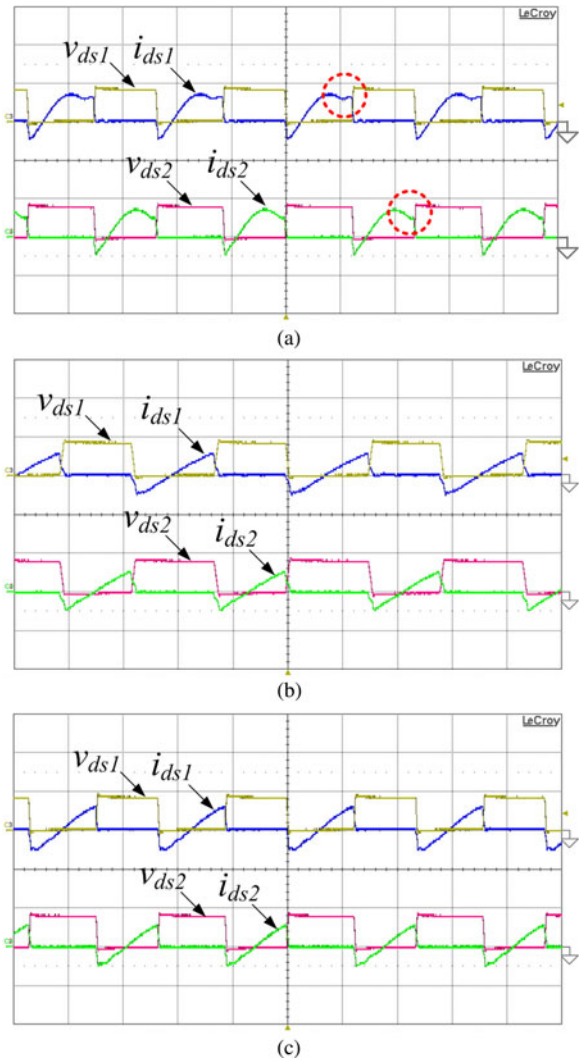

Fig. 10. Measured voltage and current waveforms of primary switches S_1 and S_2 when the proposed SAS operates at (a) point "E" (v_{ds1}, v_{ds2}: 500 V/div; i_{ds1}, i_{ds2}: 1 A/div; time: 5μs/div), (b) point "A" (v_{ds1}, v_{ds2}: 500 V/div; i_{ds1}, i_{ds2}: 1 A/div; time: 2 μs/div), and (c) point "H" (v_{ds1}, v_{ds2}: 500 V/div, i_{ds1},i_{ds2}: 1 A/div; time: 5 μs/div).

Fig. 12 shows the measured transient response to the step changes between the operation points of "E" and "G." It can be observed that the output voltage can vary according to the corresponding output current and returns to steady state within 6 ms. Fig. 13 shows the measured *V–I* curve of the proposed SAS with closed-loop control. It can be observed that the measured output characteristics are very close to the theoretical *V–I* curve obtained from (3). These results prove that the output voltage and current of the proposed SAS can be adjusted simultaneously to match the electrical characteristics of PV output.

In order to further verify the system stability, a boost converter with perturb and observe (P&O) MPPT algorithm [1], [2] and output-current feedback control is connected in series with the proposed SAS. This is one of the most popular structures to achieve MPPT feature in the PV applications. The measured frequency responses of the SAS output impedances Z_o are shown in Fig. 14, in which the curves are measured according to the

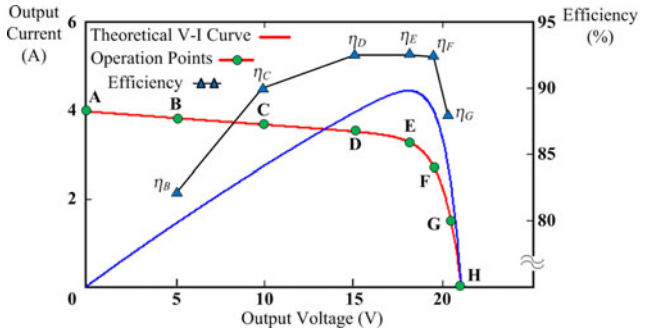

Fig. 11. Measured efficiencies of the proposed SAS according to the operation points "A" to "H."

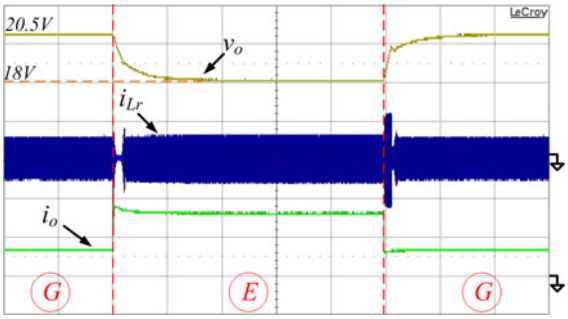

Fig. 12. Measured transient response to the step changes between the operation points of "E" and "G" (v_o: 2 V/div; i_o: 2 A/div; i_{Lr}: 1 A/div; time: 5 ms/div).

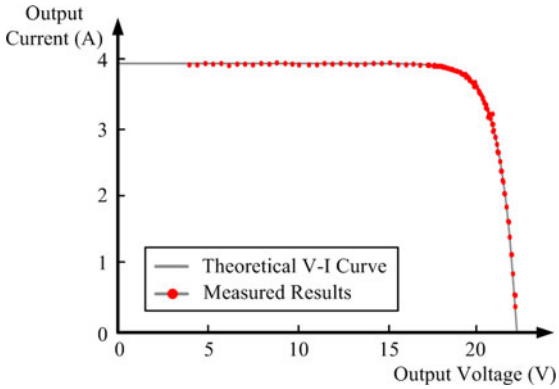

Fig. 13. Measured *V–I* curve of the proposed SAS with closed-loop control.

operation points of "D," "E," and "F." As discussed in the literature [23], the impedance ratio, defined as $T_m = Z_o/Z_{\rm in}$, can be used to determine the system stability, where $Z_{\rm in}$ is the input impedance of the boost converter. By comparing the frequency responses of Z_o with those of $Z_{\rm in}$, the simulated frequency response of T_m can be illustrated in Fig. 15. It reveals that the gain $|T_m|$ is always less than 0 dB between 1 Hz and 100 kHz so that this cascaded system can operate stably in this frequency range. Furthermore, Fig. 16 shows the measured waveforms of i_{Lr}, v_o, i_o, and P_o of the proposed SAS while the boost converter starts up and then tracks the MPP. This result validates the ability of the proposed SAS for stable operation with an authentic MPPT converter.

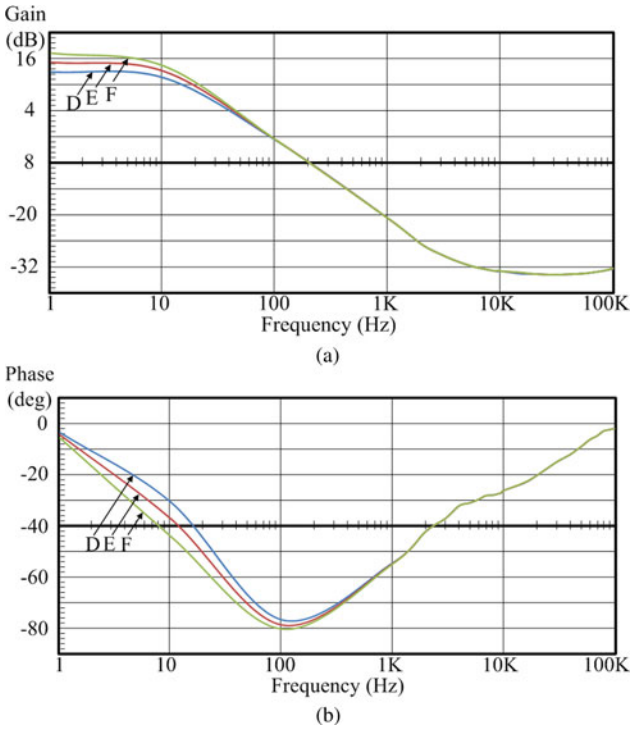

Fig. 14. Measured frequency responses of (a) gain and (b) phase of the SAS output impedances Z_o.

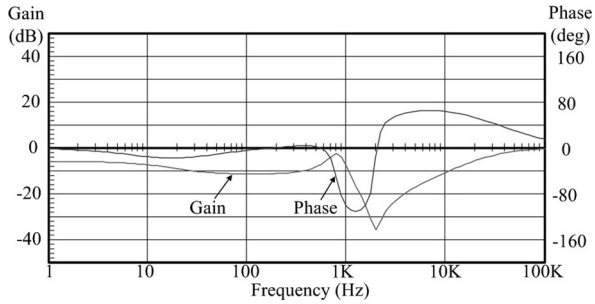

Fig. 15. Simulated frequency response of the impedance ratio T_m.

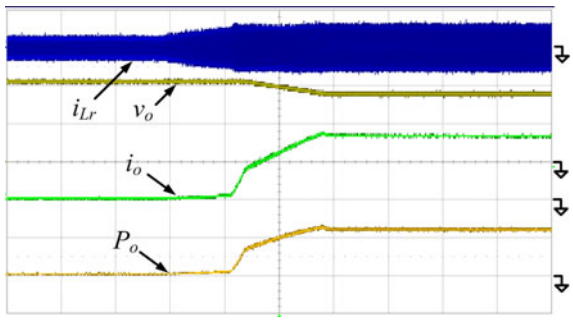

Fig. 16. Measured waveforms of i_{Lr}, v_o, i_o, and P_o of the proposed SAS while the boost converter starts up and then tracks the maximum power point (v_o: 10 V/div; i_o: 2 A/div; i_{Lr}: 1 A/div; P_o: 50 W/div; time: 500 ms/div).

VII. Conclusion

A high-efficiency SAS implemented by an *LLC* resonant converter with ZVS feature has been proposed. The detail operation principle, design procedures, and considerations are introduced.

A prototype SAS is implemented to demonstrate the feasibility and validity of the theoretical discussion. The experimental results show that the SAS can provide approximated PV output characteristics with high accuracy, and the maximum system efficiency at the range near MPP is up to around 92.5%. Hence, the proposed SAS based on an *LLC* resonant converter can significantly save the costs and energy for PV system testing, and accelerate the industrial developments of PV power.

REFERENCES

[1] N. Femia, G. Petrone, G. Spagnuolo, and M. Vitelli, "Optimization of perturb and observe maximum power point tracking method," *IEEE Trans. Power Electron.*, vol. 20, no. 4, pp. 963–973, Jul. 2005.

[2] A. K. Abdelsalam, A. M. Massoud, S. Ahmed, and P. N. Enjeti, "High-performance adaptive perturb and observe MPPT technique for photovoltaic-based microgrids," *IEEE Trans. Power Electron.*, vol. 26, no. 4, pp. 1010–1021, Apr. 2011.

[3] F. Nagamine, R. Shimokawa, M. Suzuki, and T. Abe, "New solar simulator for multi-junction solar cell measurements," in *Proc. Conf. Rec. 23rd IEEE Photovoltaic Spec. Conf.*, May 1993, pp. 686–690.

[4] S. Techajunta, S. Chirarattananon, and R. H. B. Exell, "Experiments in a solar simulator on solid desiccant regeneration and air dehumidification for air conditioning in a tropical humid climate," *Renewable Energy*, vol. 17, no. 4, pp. 549–568, Aug. 1999.

[5] A. K. Mukerjee and N. Dasgupta, "DC power supply used as photovoltaic simulator for testing MPPT algorithms," *Renewable Energy*, vol. 32, no. 4, pp. 587–592, Apr. 2007.

[6] L. A. C. Lopes and A.-M. Lienhardt, "A simplified nonlinear power source for simulating PV panels," in *Proc. IEEE Power Electron. Spec. Conf.*, Jun. 2003, pp. 1729–1734.

[7] H. Nagayoshi, "I-V curve simulation by multi-module simulator using I-V magnifier circuit," *Solar Energy Mater. Solar Cells*, vol. 82, no. 1–2, pp. 159–167, May 2004.

[8] K. Khouzam and K. Hoffman, "Real-time simulation of photovoltaic modules," *Solar Energy*, vol. 56, no. 6, pp. 521–526, Jun. 1996.

[9] J.-H. Yoo, J.-S. Gho, and G.-H. Choe, "Analysis and control of PWM converter with V-I output characteristics of solar cell," in *Proc. IEEE Int. Symp. Ind. Electron.*, Jun. 2001, vol. 2, pp. 1049–1054.

[10] P. Sanchis, J. Lopez, A. Ursua, and L. Marroyo, "Electronic controlled device for the analysis and design of photovoltaic systems," *IEEE Power Electron. Lett.*, vol. 3, pp. 57–62, Jun. 2005.

[11] M. Cirrincione, M. C. Di Piazza, M. Pucci, and G. Vitale, "Real-time simulation of photovoltaic arrays by growing neural gas controlled DC-DC converter," in *Proc. IEEE Power Electron. Spec. Conf.*, Jun. 2008, pp. 2004–2010.

[12] R. P. Severns, "Topologies for three-element resonant converters," *IEEE Trans. Power Electron.*, vol. 7, no. 1, pp. 89–98, Jun. 1992.

[13] A. K. S. Bhat, "Analysis and design of a modified series resonant converter," *IEEE Trans. Power Electron.*, vol. 8, no. 4, pp. 423–430, Oct. 1993.

[14] E. X. Yang, F. C. Lee, and M. M. Jovanovic, "Small-signal modeling of series and parallel resonant converters," in *Proc. IEEE Appl. Power Electron. Conf. Expo.*, Feb. 1992, pp. 785–792.

[15] S. D. Johnson and R. W. Erickson, "Steady-state analysis and design of the parallel resonant converter," *IEEE Trans. Power Electron.*, vol. 3, no. 1, pp. 93–104, Jan. 1988.

[16] A. K. S. Bhat, "Analysis and design of a series-parallel resonant converter," *IEEE Trans. Power Electron.*, vol. 8, no. 1, pp. 1–11, Jan. 1993.

[17] E. X. Yang, F. C. Lee, and M. M. Jovanovic, "Small-signal modeling of LCC resonant converter," in *Proc. IEEE Power Electron. Spec. Conf.*, Jun. 1992, pp. 941–948.

[18] J. F. Lazar and R. Martinelli, "Steady-state analysis of the LLC series resonant converter," in *Proc. IEEE Appl. Power Electron. Conf. Expo.*, Mar. 2001, vol. 2, pp. 728–735.

[19] B. Yang, "Topology investigation for front end DC/DC power conversion for distributed power system," Ph.D. dissertation, Dept. Elect. Comput. Eng., Virginia Polytechnic Inst. and State Univ., Blacksburg, Sep. 2003.

[20] G. Ivensky, S. Bronshtein, and A. Abramovitz, "Approximate analysis of resonant LLC DC-DC converter," *IEEE Trans. Power Electron.*, vol. 26, no. 11, pp. 3274–3284, Nov. 2011.

[21] B. Lu, W. Liu, Y. Liang, F. C. Lee, and J. D. van Wyk, "Optimal design methodology for LLC resonant converter," in *Proc. IEEE Appl. Power Electron. Conf. Expo.*, Mar. 2006, pp. 533–538.

[22] R. Beiranvand, B. Rashidian, M. R. Zolghadri, and S. M. H. Alavi, "A design procedure for optimizing the LLC resonant converter as a wide output range voltage source," *IEEE Trans. Power Electron.*, vol. 27, no. 8, pp. 3749–3763, Aug. 2012.

[23] C. M. Wildrick, F. C. Lee, B. H. Cho, and B. Choi, "A method of defining the load impedance specification for a stable distributed power system," *IEEE Trans. Power Electron.*, vol. 10, no. 3, pp. 280–285, May 1995.

Chien-Hsuan Chang (M'12) was born in Kaohsiung, Taiwan, in 1974. He received the B.S. degree in electrical engineering from the National Sun Yat-Sen University, Kaohsiung, Taiwan, in 1996, and the M.S. and Ph.D. degrees in electrical engineering from the National Chung Cheng University, Chiayi, Taiwan, in 1998 and 2002, respectively.

From 2002 to 2007, he was a Chief Engineer and Team Leader in the Department of Telecom Power Module, Acbel Polytech, Inc., Tamsui, Taipei, Taiwan, where he designed and developed high-power density and high-efficiency power modules for Telecom applications. Since February 2007, he has been in the Department of Electrical Engineering, I-Shou University, Kaohsiung, where he is currently an Assistant Professor. His current research interests include power-electronic converters and their applications on photovoltaic power systems and LED drivers.

En-Chih Chang was born in Kaohsiung, Taiwan, in 1975. He received the B.S. degree from Feng-Chia University, Taichung, Taiwan, in 1999, the M.S. degree from National Taiwan Ocean University, Keelung, Taiwan, in 2001, and the Ph.D. degree from National Cheng Kung University, Tainan, Taiwan, in 2008, all in electrical engineering.

He joined the Department of Electrical Engineering, I-Shou University, Kaohsiung, Taiwan, in 2009 as an Assistant Professor. His research interests include sliding mode control, intelligent control, grey theory, and their applications in power electronics systems.

Hung-Liang Cheng (M'08) was born in Chunghwa, Taiwan, in 1964. He received the B.S., M.S., and Ph.D. degrees in electrical engineering from the National Sun Yat-Sen University, Kaohsiung, Taiwan, in 1986, 1988, and 2001, respectively.

From 1988 to 2007, he was an Electronic Researcher at the Chung-Shan Institute of Science and Technology, Taoyuan County, Taiwan, where he designed and developed high-power transmitters in radar and missile systems. Since February 2007, he has been in the Department of Electrical Engineering, I-Shou University, Kaohsiung, where he is currently an Associate Professor. His current research interests include power electronic converters and electronic ballasts/drivers for lighting applications.